UC Merced

UC Merced Previously Published Works

Title

Incoherent source localization in random acoustic waveguides

Permalink

https://escholarship.org/uc/item/0zx338j4

Journal

Waves in Random and Complex Media, 30(1)

ISSN

1745-5030

Authors

Borcea, L
Karasmani, E
Tsogka, C

Publication Date

2020-01-02

DOI

10.1080/17455030.2018.1486052

Peer reviewed

eScholarship.org Powered by the California Digital Library
University of California

Incoherent source localization in random acoustic waveguides

L. Borcea
Department of Mathematics, University of Michigan, Ann Arbor, MI 48109

E. Karasmani
Institute of Applied and Computational Mathematics (IACM),
Foundation for Research and Technology - Hellas, Heraklion 70013, Greece

C.Tsogka*
Applied Math Unit, University of California, Merced,
5200 North Lake Road, Merced, CA 95343

February 4, 2020

Abstract

We consider the problem of localizing one or more sources in a two-dimensional waveguide with horizontal flat boundaries and random sound speed fluctuations. Our data is the acoustic pressure field, measured on a vertical array of hydrophones that may span the entire depth of the waveguide or a part of it. We use randomness to model the effect of internal waves on the sound channel. Although the strength of the fluctuations is small, the transmitted signal is significantly affected from the multiple scattering of the waves with the random inhomogeneities, especially since we consider large propagation distances between the sources and the receiver array. Source localization is performed following an incoherent approach relying on a transport system of equations that describes wave propagation in random waveguides and that takes into account modal dispersion and energy transfer between modes.

Keywords: acoustic waveguides; source localization; random media

1 Introduction

We consider the problem of multiple source detection and localization in a sea environment with fluctuations in the sound speed profile caused by internal waves as in [1, 2]. The fluctuations depend on the direction of propagation, called the range, as well as on the vertical depth direction. The strength of the fluctuations, ε, is small but we consider very long distances of propagation between the sources and the vertical array of hydrophones on which the acoustic pressure field $p(t, \vec{x})$ is recorded. In such regimes cumulative scattering due to the medium inhomogeneities becomes important and $p(t, \vec{x})$ loses its coherence. This means that its expectation with respect to the realizations of the random medium, $\langle p(t, \vec{x}) \rangle$, decays exponentially with the propagation distance on the scale of the scattering mean free path and becomes small with respect to the fluctuations $p(t, \vec{x}) - \langle p(t, \vec{x}) \rangle$. It is therefore a regime in which coherent imaging methods fail [3].

*Corresponding author. Email: ctsogka@ucmerced.edu

It is well known that in random acoustic waveguides the modes are coupled through the random medium fluctuations and there is transfer of energy between modes due to scattering [1, 4, 2]. In the review paper [5] which considers long range basin scale observations it is shown that narrow-band and broad-band signals are affected in a different way when propagating in the random ocean. Another important factor that should be taken into account to more accurately describe shallow-water wave propagation is the presence of energy absorbing sub-bottom sediment layers as in [6, 7]. We also refer the reader to the recent book [8] for a review of ocean wave propagation through random media theory.

We consider here an idealized marine environment with flat horizontal boundaries and a hard bottom boundary condition. The deterministic velocity profile we use is depth dependent and the fluctuations of the sound speed are two-dimensional. Although this is a simplified and rather ideal model of a marine acoustic environment it still carries and exhibits the main features and challenges appearing in the problem of source localization in the sea. As it was shown in [3] the behavior of source localization methods depends primarily on the statistics of the propagating modes and for long propagation distances coherent imaging fails. We refer also to [9] where coherent source imaging was considered for two types of random waveguides: with fluctuations in the waveguide boundaries or in the interior. In the random boundary case, the scattering mean free path is much longer for the lower modes. Therefore successful coherent imaging can be achieved after introducing weights with which each mode should be included in the imaging procedure. By reducing the weights of the higher modes stability is gained but also resolution deteriorates. Optimal weights can be computed so as to achieve an optimal trade-off between loss of resolution and stability. However, this does not help in the case of internal inhomogeneities since in this case all the modes become incoherent at similar scales. This means that the scattering mean free paths are of the same order for all propagating modes and therefore coherent imaging cannot be improved by using weights and an incoherent approach should be used.

We follow in this paper the incoherent source localization methodology proposed and analyzed in [3, 10] and further developed in [11]. This methodology uses the theory in [12, 4] and [13] to derive a stochastic system of differential equations for the modal amplitudes. More precisely, under the assumptions of diffusion and forward scattering approximation, in the asymptotic scale of small fluctuations and long propagation distances, a system of transport equations is derived. This system describes how mode coupling and transfer of energy between modes occurs in random waveguides (see also [14] and [15]). Taking into account this system of transport equations an incoherent approach for the source inverse problem has been developed [3, 16, 11].

In this work we focus on the generalization of this incoherent source localization methodology to the case of multiple sources, as well as, depth dependent velocity profiles. We carefully design our numerical experiments and use them in order to assess the performance of the incoherent methodology. In particular, to simulate a sea water environment we use a numerical model for a waveguide with a rigid bottom and a mean sound speed profile coming from the YELLOW SHARK '94 experiment [17]. To model inhomogeneities due to internal waves we add to this profile, depth and range dependent random fluctuations at the scale of the wavelength. We consider wave propagation in regimes close to and beyond the equipartition distance, that is the distance at which energy is uniformly distributed between the modes, independently of the initial state. Source localization in such regimes is very challenging.

The key ingredient for the inversion is the dispersion function which expresses the fact that the energy carried by different modes propagates with a different speed in the random medium compared to the deterministic unperturbed case. This difference in the transport speed can be explained from the asymptotic theory and an analytic form for the dispersion function is derived. Using a model for the medium's correlation function we essentially reduce our source localization problem to the estimation of four parameters: the propagation distance, the depth of the source, the amplitude and the correlation length of the random fluctuations.

We illustrate with simulated, incoherent data that the inversion methodology is very accurate, and stable with respect to the realizations of the random medium. The source range is recovered, even in the case of only two receivers (see also [18]). It is not important to know the exact form of the correlation function of the medium, and very good range estimation is obtained even when the wrong model is used. Depth estimation is more delicate, and good results are obtained only when larger bandwidths are used. In that case too we rely on the dispersion function and assume that the source range has been already recovered.

In this paper the data used for the inversion are derived by solving the full acoustic wave equation in two dimensions and this is certainly a very time consuming process. However, it allows us to check our inversion approach without committing the inverse crime, that means without having perfect data that follow exactly the model used in the inversion procedure. Novel approaches relying on random matrix theory as the one developed in [19] look very promising and time efficient. It would be very interesting to investigate the use of such approaches in combination with our inversion methodology.

The paper is organized as follows. In Section 2 we give the mathematical formulation for the source localization problem. In Section 3 we describe briefly two coherent imaging methods and in Section 4 we show that they both fail to locate the sources in the wave propagation regime considered in this paper. In Section 5 the incoherent methodology for estimating the source location is presented and in parallel its performance is illustrated with numerical simulations. In Section 6 we place in context the model for the random waveguide used and summarize the results. The main conclusions of this work are recovered in Section 7. A description of the model used in the incoherent methodology, which is an asymptotic model for wave propagation in random waveguides, is given in Appendix A.

2 Formulation of the Source localization Problem

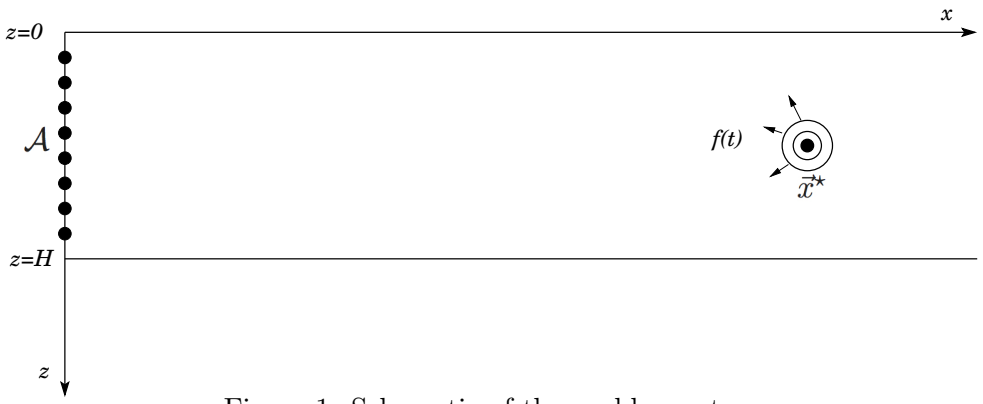

Figure 1: Schematic of the problem setup.

We consider acoustic wave propagation in a two dimensional inhomogeneous waveguide with planar horizontal boundaries as the one depicted in Figure 1. The acoustic pressure field $p(t,\vec{x}) = p(t,x,z)$ is governed by the scalar wave equation

$$\Delta p(t,x,z) - \frac{1}{c^2(x,z)}\frac{\partial^2 p(t,x,z)}{\partial t^2} = F(t,x,z), \tag{1}$$

with a pressure release boundary condition at the surface

$$p(t,x,z) = 0, \quad z = 0,$$

and a rigid bottom

$$\frac{\partial p(t,x,z)}{\partial z} = 0, \quad z = H.$$

While this simplified model problem does not adequately describe most shallow-water environments, it suffices for illustrating the difficulties in the source localization problem resulting from random volume inhomogeneities. We assume a source term in Eq.(1) of the form

$$F(t,x,z) = f(t)\rho(x,z),$$

which models a source with density $\rho(x,z)$ emitting a pulse $f(t)$ towards a vertical receiver array $\mathcal{A}$, located at $x_{\mathcal{A}}$. Note that we use a coordinate system with range origin at the array and assume that propagation is from right to left. The pulse has a central frequency f_0 and is supported in the frequency band $[f_0 - B, f_0 + B]$. We call B the bandwidth and we assume that $\frac{f_0}{B} \in [0.1, 1]$ so that we can consider both the narrowband and the broadband cases.

We denote Ω_ρ the support of the source, a domain centered at $\vec{x}^\star = (x^\star, z^\star)$. When multiple ($n_s$) sources are considered the source term is of the form,

$$F(t,x,z) = \sum_{j=1}^{n_s} f_j(t)\rho_j(x,z).$$

with Ω_{ρ_j} the support of $\rho_j(x,z)$ centered at $\vec{x}_j^\star = (x_j^\star, z_j^\star)$ for $j = 1, \ldots, n_s$.

We want to model sea water with internal waves caused by changes in temperature and salinity. In such environments the sound speed $c(x,z)$ has an (x,z) dependent fluctuating part (see [1] and [4]) that can be modeled by

$$\frac{c_0^2(z)}{c^2(x,z)} = 1 + \varepsilon\nu\left(\frac{x}{\ell}, \frac{z}{\ell}\right), \tag{2}$$

where $c_0(z)$ is the unperturbed velocity profile corresponding to $\varepsilon = 0$. Here $\nu\left(\frac{x}{\ell}, \frac{z}{\ell}\right)$ is an isotropic, statistically homogeneous random process with mean zero and integrable in range correlation function,

$$\mathcal{R}(\vec{x}, \vec{x}') = \left\langle \nu\left(\frac{x}{\ell}, \frac{z}{\ell}\right), \nu\left(\frac{x'}{\ell}, \frac{z'}{\ell}\right) \right\rangle.$$

The perturbation parameter, ε, is small and ranges between 1% and 3%. The length scale, ℓ, is the correlation length of the fluctuations and it is assumed here to be of the order of the wavelength. Although the fluctuations are weak, after multiple interactions of the waves with the medium heterogeneities the cumulative effect on the pressure field is important, especially for waves that travel over long distances in the waveguide.

The source localization problem that we want to solve is to estimate the number n_s and the locations $\vec{x}_j^\star$, $j = 1, \ldots, n_s$, of the sources, in range and depth, given the observed acoustic pressure field $p^{obs}(t, x_{\mathcal{A}}, z_r)$ on the array $\mathcal{A}$. The observed pressured field could be obtained either by experimental measurements or by numerical simulation.

3 Coherent Imaging

We define here two coherent imaging functions. We will illustrate in the next section how they fail to give useful results in wave propagation regimes where the cumulative scattering by the random medium inhomogeneities is strong.

The first coherent imaging function is given by

$$\mathcal{I}(\vec{x}^s) = \int \frac{d\omega}{2\pi} \sum_{z_r \in \mathcal{A}} \widehat{p}^{\,*}(\omega, x_{\mathcal{A}}, z_r) \widehat{G}_0(\omega, x_{\mathcal{A}}, z_r; \vec{x}^s), \tag{3}$$

where * denotes complex conjugation and $\widehat{G}_0(\omega, x, z; \vec{x}^s)$ is the Green's function for the Helmholtz equation in the unperturbed waveguide between points $\vec{x}^s$ and (x, z) at circular frequency ω. Here $\vec{x}^s$ denotes the search point that takes values in the imaging window at which we evaluate the imaging function $\mathcal{I}(\vec{x}^s)$. Eq. (3) can be interpreted as the back-propagation of the recorded pressure field from each receiver on the array $(x_{\mathcal{A}}, z_r)$ to the hypothetical source location $\vec{x}^s$. In the absence of the random fluctuations, the back-propagation performed in $\mathcal{I}(\vec{x}^s)$ is exact since the Green's function $G_0(\omega, x_{\mathcal{A}}, z_r; \vec{x}^s)$ is the correct Green's function in the background medium. In that case $\mathcal{I}(\vec{x}^s)$ produces an image that has a peak at the correct source location $\vec{x}^s = \vec{x}^\star$.

The second method we consider is Coherent INTerferometry (CINT) that was introduced in [20, 21] for imaging in random, open environments. CINT back propagates to $\vec{x}^s$ cross correlations of the acoustic pressure field recorded at the array, instead of back-propagating the recorded pressure field as in $\mathcal{I}(\vec{x}^s)$. The cross correlations are over suitable time and receiver offset windows, and they introduce a statistical smoothing in the imaging process for achieving stability [22]. The optimal smoothing is determined by two decoherence parameters intrinsic to the data: the decoherence length Z_d and frequency Ω_d [21, 22]. The decoherence length is the receiver offset $|z_r - z_{r'}|$ over which $\widehat{p}(\omega, x_{\mathcal{A}}, z_r)$ and $\widehat{p}(\omega, x_{\mathcal{A}}, z_{r'})$ become statistically uncorrelated. Similarly, Ω_d is the frequency lag $|\omega - \omega'|$ over which $\widehat{p}(\omega, x_{\mathcal{A}}, z_r)$ and $\widehat{p}(\omega', x_{\mathcal{A}}, z_r)$ become uncorrelated. It follows from [12, 4, 13] that in random waveguides, at long source-array ranges, there is no decorrelation over the receiver offset, but there is rapid decorrelation over the frequency (Ω_d is small). Thus, CINT reduces to back propagating the cross correlation of the received pressure field across the array, over long time windows of support $(2\Omega_d)^{-1}$,

$$\begin{aligned} \mathcal{I}^{CINT}(\vec{x}^s) = \int_{|\omega-\omega_0|\le 2\pi B} \frac{d\omega}{2\pi} \int_{|\omega-\omega'|\le 2\pi\Omega_d} \frac{d\omega'}{2\pi} \sum_{z_r \in \mathcal{A}} \widehat{p}(\omega, x_{\mathcal{A}}, z_r) \widehat{G}_0^*(\omega, x_{\mathcal{A}}, z_r; \vec{x}^s) \\ \times \sum_{z_{r'} \in \mathcal{A}} \widehat{p}^{\,*}(\omega', x_{\mathcal{A}}, z_{r'}) \widehat{G}_0(\omega', x_{\mathcal{A}}, z_{r'}; \vec{x}^s). \end{aligned} \tag{4}$$

The CINT imaging function behaves better than the backpropagation method of Eq.(3) and its expected value does not decay exponentially with range as is the case for Eq.(3). However, due to the dispersion induced by the random medium fluctuations, it does not give reliable results in the incoherent wave propagation regime considered in this paper. For a detailed theoretical analysis of the resolution and stability properties of these two methods we refer the interested reader to [3].

There are other imaging methods that employ signal processing tools for mitigating additive noise [23]. As long as these methods rely on a coherent $p(t, x_{\mathcal{A}}, z_r)$ (or $\widehat{p}(\omega, x_{\mathcal{A}}, z_r)$), they are not expected to give reliable results when $p(t, x_{\mathcal{A}}, z_r)$ becomes incoherent as is the case for the numerical simulations considered in the next section. It would be interesting to examine how the adaptive normal mode back-propagation method proposed in [24] performs with incoherent data such as the ones considered next. However this is beyond the scope of the present paper.

4 Numerical simulations

In this paper, we obtain the observed field $p^{obs}(t, x_{\mathcal{A}}, z_r)$ (data) by computing numerically the solution of the time dependent wave equation as a first order velocity-pressure system using the finite element method described in [25] coupled with two perfectly matched layers (PMLs) [26] on the vertical boundaries of the waveguide.

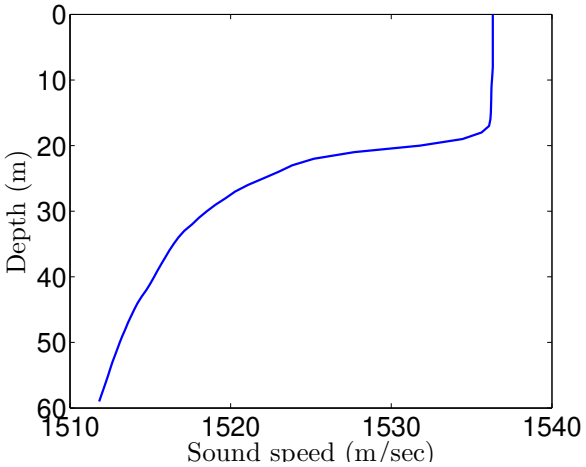

Figure 2: The sound speed profile.

We choose either a constant background speed profile with $c_0 = 1500$m/s or the depth dependent $c_0(z)$ shown in Figure 2. This variable sound speed profile is coming from the YELLOW SHARK '94 experiment in South Elba, in Italy, cf. [17]. We take fluctuations of the sound speed as in Eq.(2) with $\varepsilon = 2\%$ or 3%, using a Gaussian correlation function

$$\mathcal{R}_G(\vec{x}, \vec{x}') = \alpha e^{-\frac{|x-x'|^2+|z-z'|^2}{2\ell^2}}. \tag{5}$$

We generate the process ν numerically using random Fourier series [27]. For each source configuration, we compute eight data sets corresponding to different realizations of the random medium. The correlation length is $\ell = 0.5\lambda_c$ with $\lambda_c = c_0/f_c$ the wavelength and f_c the central frequency. The amplitude of the Gaussian is $\alpha = 1$.

The depth of the waveguide is $H = 20\lambda_c$ and our data are computed on an array with 201 equidistant receivers, with the first and last receiver of the array being $\lambda_c/4$ far from the horizontal and flat boundaries of the considered waveguide. We use data either with two unknown sources, one at $\vec{x}_1^\star = (15\lambda_c, 393\lambda_c)$ and the other at $\vec{x}_2^\star = (5\lambda_c, 493\lambda_c)$ or with one source at $\vec{x}_2^\star$. The direct arrival from the source at $\vec{x}_2^\star$ to the array in a homogeneous waveguide is at time $x_2^\star/c_0 = 0.986$s. The data are computed in the time window $t \in (0, 6.3306)$s.

The source excitation used is a Ricker wavelet

$$f(t) = -2\pi^2 f_c^2 (1 - 2(t-t_0)^2 \pi^2 f_c^2) \exp\left(-\pi^2 f_c^2 (t-t_0)^2\right)$$

with central frequency $f_c = 500$Hz and $t_0 = 1/f_c$. This pulse is mainly supported in the frequency range $50 - 950$Hz. For the case of the two sources we have used the same pulse for both sources (same strength, phase and frequency). The Fourier coefficients $\widehat{p}^{obs}(\omega, x_{\mathcal{A}}, z_r)$ of the data are computed using the Fast Fourier Transform algorithm. For the source localization we will consider data in sub-bands $[f_0 - B, f_0 + B]$ for $B = 62.5$Hz and for different values of f_0 to study how the central frequency affects the results. We will also consider data for several sub-bands to study the effect of a larger bandwidth.

For the density of the source, in the numerical simulations we have used

$$\rho^e(x, z) = e^{-\frac{|x-x^\star|^2+|z-z^\star|^2}{2\sigma_e^2}},$$

with $\sigma_e = \sqrt{2}\lambda_c/20$.

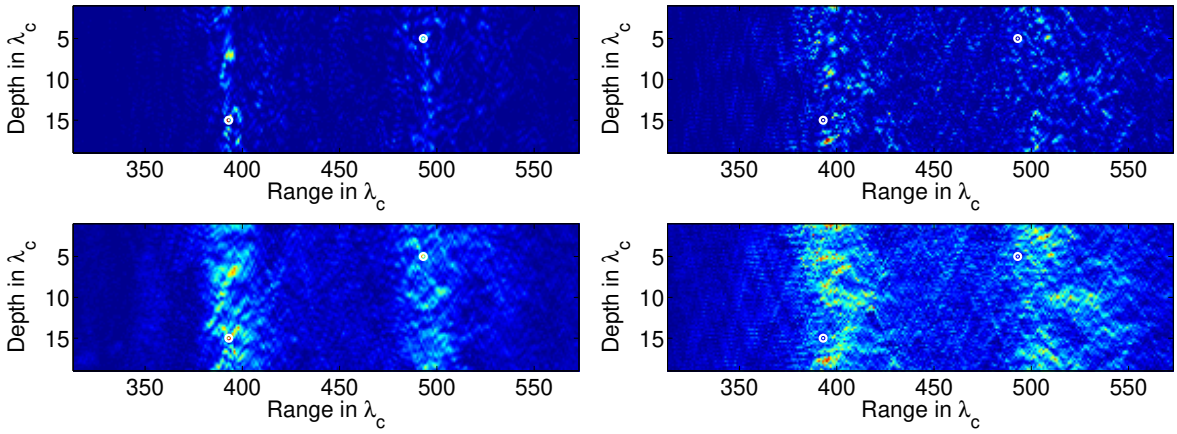

Figure 3: $\mathcal{I}(\vec{x}^s)$ (top row) and $\mathcal{I}^{CINT}(\vec{x}^s)$ (bottom row), with $f_0 = 500$Hz, $\varepsilon = 2\%$ (left) and $f_0 = 887$Hz, $\varepsilon = 3\%$ (right). The bandwidth is $B = 62.5$Hz and $\Omega_d = 14.8$Hz. Data for two sources and the variable sound speed profile. The correct source location is indicated with a white circle.

In Figures 3 and 4 we present the images obtained with the two coherent functionals $\mathcal{I}(\vec{x}^s)$ and $\mathcal{I}^{CINT}(\vec{x}^s)$ for the simulated data. We compute the functionals in Eqs. (3) and (4), using $\widehat{p} = \widehat{p}^{obs}$.

In Figure 3 we use the data for the two sources and the variable sound speed profile. The bandwidth is $B = 62.5$Hz and $\Omega_d = 14.8$Hz. On the left plots we show results at $f_0 = 500$Hz with $\varepsilon = 2\%$ (close to the equipartition distance defined in Eq. (25), see also Figure 12-left) and on the right at $f_0 = 887$Hz with $\varepsilon = 3\%$ (beyond the equipartition distance, see Figure 12-right). The range interval contains both sources ($[315{,}575]\lambda_c$). We take a step of λ_c in range and $\lambda_c/4$ in depth. The correct value of the sources' location is indicated with a white circle. We show here results for one realization of the random medium but the results are similar for other realizations of the medium fluctuations. We observe that both coherent methods fail to locate the sources correctly. A rough estimation about range may be obtained but the images look noisy and have several spurious peaks. As the frequency and/or the strength of the fluctuations increases, determining the sources' location becomes more challenging.

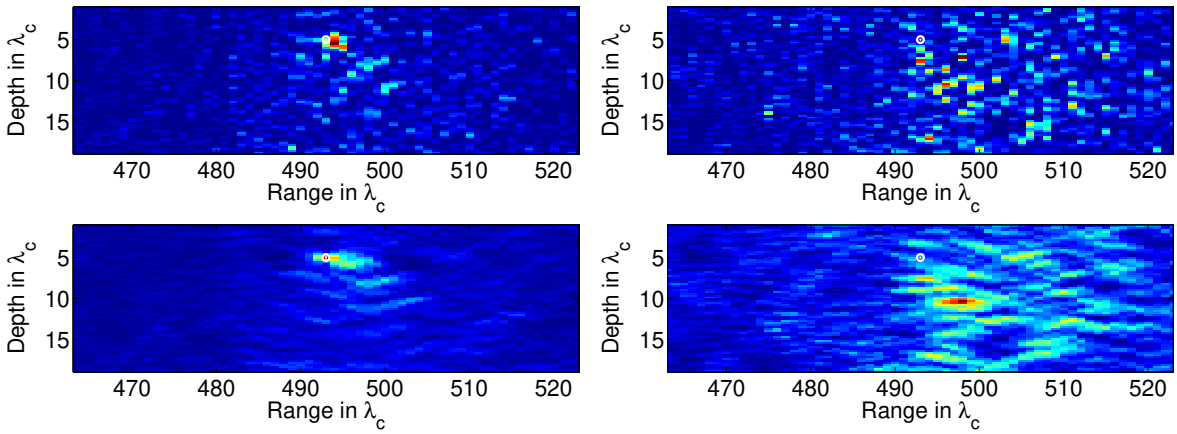

Figure 4: $\mathcal{I}(\vec{x}^s)$ (top row) and $\mathcal{I}^{CINT}(\vec{x}^s)$ (bottom row), with $\varepsilon = 2\%$ (left) and 3% (right), at $f_0 = 600$Hz. The bandwidth is $B = 212.5$Hz and $\Omega_d = 50$Hz. Data for one source and the constant sound speed profile. The correct source location is indicated with a white circle.

In Figure 4 we use the data for one source located at $\vec{x}_2^{\star} = (5\lambda_c, 493\lambda_c)$ for a constant sound speed profile. We use now a larger bandwidth $B = 212.5$Hz, $\Omega_d = 50$Hz and central frequency $f_0 = 600$Hz. We show results with $\varepsilon = 2\%$ (on the left plots) and 3% (on the right plots). We display the image for a shorter range interval [463,523]λ_c. The imaging window dicsretization steps are as before. We observe that despite the large bandwidth used, both coherent methods fail to locate the source correctly when we increase the strength of the fluctuations from $\varepsilon = 2\%$ to 3%. We will present in the next section an incoherent source localization methodology that provides robust results in this challenging wave propagation regime.

5 Incoherent Source Localization Methodology

We assume that the density of the source is of separable form $\rho(x, z) = \xi(z)\eta(x)$ and seek to extract information about the functions $\xi(z)$ and $\eta(x)$. Since the source is located at a large distance from the array, of the order of hundreds of wavelengths, the range profile of the source can be accurately approximated by a delta function at the correct range, $\eta(x) \approx \delta(x)$. We want to estimate the range of the sources x_j^{est} and their depth profiles $\xi_j^{\text{est}}(z)$. Concerning the depth profile we will see below that we can invert for the absolute values of its Fourier coefficients defined by

$$\widehat{\xi}_j = \int_0^H dz\, \xi(z)\phi_j(\omega_0, z), \quad j = 1, \dots N, \tag{6}$$

with $N := N(\omega_0)$ the number of propagating modes, ϕ_j, in the unperturbed waveguide (see Appendix A) and ω_0 being the central frequency of the considered bandwidth.

We first project the Fourier coefficients of the acoustic pressure field on the array onto the propagating modes and define

$$\widehat{P}_j(\omega, x_{\mathcal{A}}) = \sum_{z_r \in \mathcal{A}} \widehat{p}(\omega, x_{\mathcal{A}}, z_r)\phi_j(\omega, z_r), \quad j = 1, \dots N.$$

Then by taking the cross-correlations of $\widehat{P}_j(\omega)$ over long time windows of support $(2\Omega_d)^{-1}$ we compute the following function which we call dispersion function

$$\mathcal{D}_j(\chi) = \int_{|\omega-\omega_0|\le 2\pi B} \frac{d\omega}{2\pi} \int_{|\omega-\omega'|\le 2\pi\Omega_d} \frac{d\omega'}{2\pi}\, \widehat{P}_j(\omega, x_{\mathcal{A}})\widehat{P}_j^*(\omega', x_{\mathcal{A}})e^{-i(\beta_j(\omega)-\beta_j(\omega'))\chi}, \tag{7}$$

where $\chi = \tau/\beta_j'(\omega_0)$ with $\beta_j'(\omega)$ the derivative of $\beta_j(\omega)$ with respect to ω, τ being the arrival time and Ω_d the decoherence frequency, that is the frequency lag $|\omega - \omega'|$ over which $\widehat{P}_j(\omega)$ and $\widehat{P}_j(\omega')$ become uncorrelated. The decoherence frequency Ω_d is a-priori unknown as it depends on the statistical properties of the random medium. It can be estimated directly from the data using statistical signal processing techniques like the variogram [28]. However, optimal imaging results are obtained when Ω_d is estimated during the image formation process as in adaptive CINT [21]. Here we follow the latter approach.

In an unperturbed waveguide ($\varepsilon = 0$), for all modes j the $\mathcal{D}_j(\chi)$ are aligned and they all peak at the same location which corresponds to the range of the source X. In a random medium, however, each $\mathcal{D}_j(\chi)$ peaks at a different χ_j, which in general is not equal to X. This is a form of dispersion with respect to the modes and is due to the fact that in the random waveguide the transport speed is not $\beta_j'(\omega)$. We will use this dispersion function for estimating the sources' location.

To do so, we substitute the Fourier coefficients $\widehat{p}^{obs}$ of the observed field p^{obs} into Eq.(7) and obtain the dispersion function for the data, $\mathcal{D}_j^{obs}$. Moreover, using the asymptotic model for the random

waveguide (described in Appendix A and derived under the diffusion approximation and neglecting backscattering, in the asymptotic scale of small fluctuations and long propagation distances) we deduce the following theoretical expression for the dispersion function

$$\mathcal{D}_j^{mod}(\chi; X^s) \approx \sum_{q,l=1}^{N} \frac{|\widehat{\xi}_l|^2}{\beta_l \beta_q} Q_{jq}^2 \mathcal{W}_q^{(l)}(\omega_0, \beta_j' \chi, X^s), \tag{8}$$

where

$$\mathcal{W}_q^{(l)}(\omega_0, \beta_j' \chi, X^s) = \int \frac{dh}{2\pi} \widehat{\mathcal{W}}_q^{(l)}(\omega_0, h, X^s) e^{-ih\beta_j' \chi},$$

is the inverse Fourier transform of Eq.(21) and X^s the hypothetical scaled range of the source that we seek to determine. Here we have assumed a small bandwidth, so that $N(\omega) \approx N(\omega_0) = N$ and $\beta_j(\omega) \approx \beta_j(\omega_0) = \beta_j$, for $j = 1, \dots N$. Note that we have introduced Q, the mode coupling matrix on the array $\mathcal{A}$ with entries

$$Q_{jq} = \int_{\mathcal{A}} dz \phi_j(z) \phi_q(z). \tag{9}$$

Remark 1 *In the data dispersion function $\mathcal{D}_j^{obs}$ we consider cross-correlations of $\widehat{p}^{obs}$ projected onto the waveguide modes. Phase information appears as the difference $(\beta_j(\omega) - \beta_j(\omega'))\chi$ in the dispersion function (see Eq.(7)). In the model dispersion function $\mathcal{D}_j^{mod}$ only the central circular frequency ω_0 of the source's pulse appears, as can be seen from Eq.(8). Phase information is contained in the second argument of $\mathcal{W}_q^{(l)}$ which is evaluated at $\beta_j' \chi$.*

5.1 Range estimation methodology

By comparing the theoretical model $\mathcal{D}_j^{mod}$ with the data $\mathcal{D}_j^{obj}$ an estimation for the range location of the source is obtained. As pointed out in [11], this method is basically an arrival time analysis which takes into account the modal dispersion. Although the model Eq.(8) depends on the absolute value of the Fourier coefficients $|\widehat{\xi}_j|$ (defined in Eq.(6)), range estimation is not really affected by the value of $|\widehat{\xi}_j|$ which can be replaced by a constant in Eq.(8).

What really affects $\mathcal{D}_j^{mod}$ is the matrix $\Gamma = \Gamma(\omega_0)$ which is a-priori unknown since it depends on the correlation function of the medium's fluctuations. We can however use a parametric model, such as the Gaussian correlation function in Eq.(5) with amplitude α and correlation length ℓ, and estimate the model's parameters as well as the unknown range X of the source by minimizing the following objective function over the search space (X^s, ℓ^s, α^s)

$$\mathbb{O}_{\mathcal{D}}(X^s, \ell^s, \alpha^s) = \sum_{j \in \mathcal{S}} \int_{\chi_1}^{\chi_2} d\chi \left| \frac{\mathcal{D}_j^{obs}(\chi)}{\mathcal{D}_j^{obs}(\chi_j)} - \frac{\mathcal{D}_j^{mod}(\chi; X^s, \ell^s, \alpha^s)}{\mathcal{D}_j^{mod}(\chi_j^{mod}; X^s, \ell^s, \alpha^s)} \right|^2, \tag{10}$$

where

$$\mathcal{D}_j^{obs}(\chi_j) = \max_{\chi} \left| \mathcal{D}_j^{obs}(\chi) \right|$$

and

$$\mathcal{D}_j^{mod}(\chi_j^{mod}; X^s, \ell^s, \alpha^s) = \max_{\chi} \left| \mathcal{D}_j^{mod}(\chi; X^s, \ell^s, \alpha^s) \right|.$$

The set $\mathcal{S}$ of the modes used in Eq.(10) is determined by $\mathcal{D}_j^{obs}(\chi_j) > \delta$, with δ a user defined tolerance. The integral in χ in Eq.(10) is computed over the range interval of interest $[\chi_1, \chi_2]$. An adaptive refinement approach is followed, where at first we scan a large range interval with a big discretization

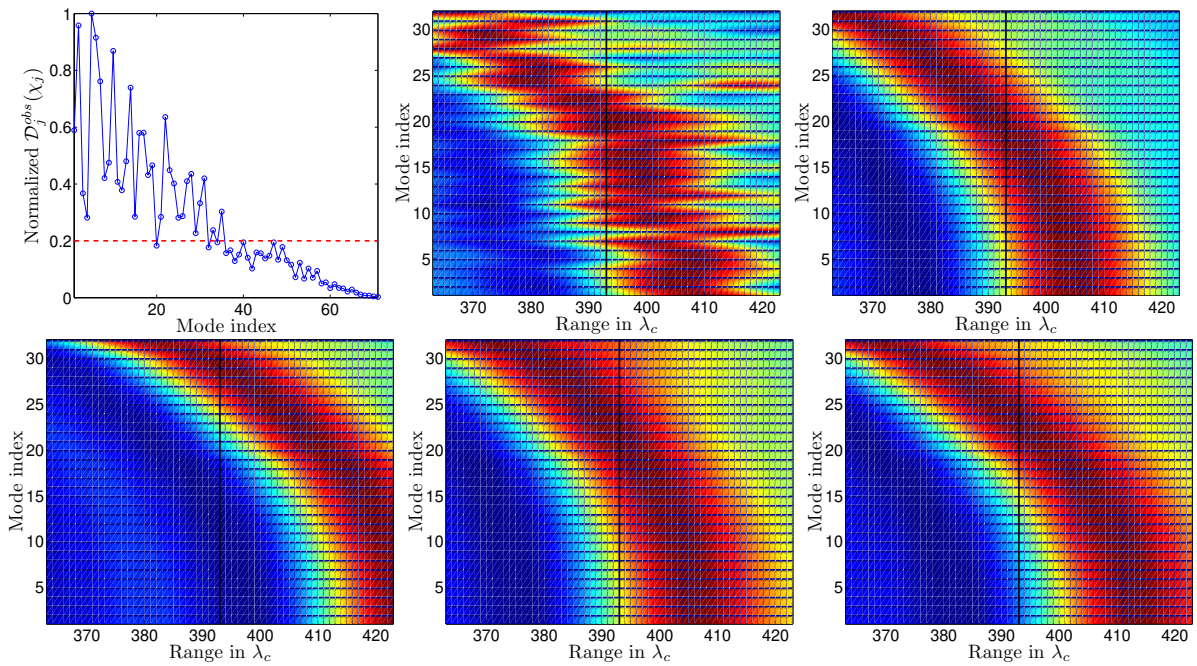

Figure 5: Results for the source at $\vec{x}_1^{\star}$ with $f_0 = 887$Hz and $\varepsilon = 3\%$. Data for two sources and the constant sound speed profile. **Top row:** Left: Normalized $\mathcal{D}_j^{obs}(\chi_j)$ and the threshold $\delta = 0.2$ for determining the set $\mathcal{S}$ of indexes. Middle: $\mathcal{D}_j^{obs}(\chi)/\mathcal{D}_j^{obs}(\chi_j)$. Right: $\mathcal{D}_j^{mod}(\chi; X, \ell, \alpha)/\mathcal{D}_j^{mod}(\chi_j^{mod}; X, \ell, \alpha)$ with $X = \varepsilon^2 393\lambda_c$, $\ell = 0.5\lambda_c$, $\alpha = 1m^2$, the correct values of the unknown parameters. **Bottom row:** $\mathcal{D}_j^{mod}(\chi; X^s, \ell^s, \alpha^s)/\mathcal{D}_j^{mod}(\chi_j^{mod}; X, \ell, \alpha)$ for the correct values of the parameters, unless specified otherwise. Left: $X^s = X + \varepsilon^2 20\lambda_c$. Middle: $\ell^s = \ell/2.5$. Right: $\alpha^s = 2.5\alpha$.

step, and then, after the source(s) location is approximately determined, we narrow the search in a small window around the detected range using a finer discretization step.

The cost function in Eq.(10) measures the discrepancy between the dispersion function $\mathcal{D}_j^{obs}(\chi)$ coming from the data and $\mathcal{D}_j^{mod}(\chi; X^s, \ell^s, \alpha^s)$ which comes from our asymptotic model. To illustrate their behavior we plot in Figure 5 the data and the model dispersion functions for the source at $\vec{x}_1^{\star}$ with $f_0 = 887$Hz and $\varepsilon = 3\%$. We used here the data for the two sources and the constant sound speed profile. The bandwidth is $B = 62.5$Hz and $\Omega_d = 14.8$Hz. In the top left plot in Figure 5 we show how $\mathcal{D}_j^{obs}(\chi_j)$ varies with the mode index j and indicate the threshold value $\delta = 0.2$ that defines the set $\mathcal{S}$ to be used in the estimation. The set $\mathcal{S}$ contains the mode indexes j with peak amplitudes above this threshold. The middle picture in the top row is a plot of $\mathcal{D}_j^{obs}(\chi)/\mathcal{D}_j^{obs}(\chi_j)$, for $j \in \mathcal{S}$. The abscissa in the plot is $\varepsilon^{-2}\chi$ in units of λ_c. The ordinate is the mode index in $\mathcal{S}$. Note how the dispersion effects induced by the random medium causes $\mathcal{D}_j^{obs}(\chi)/\mathcal{D}_j^{obs}(\chi_j)$ to peak at different ranges than the true one, indicated by the vertical black line. The right picture in the top row of Figure 5 shows $\mathcal{D}_j^{mod}(\chi; X, \ell, \alpha)/\mathcal{D}_j^{mod}(\chi_j^{mod}; X, \ell, \alpha)$, with $X = \varepsilon^2 393\lambda_c$, $\alpha = 1m^2$, $\ell = 0.5\lambda_c$, the correct values of the unknown parameters for $j \in \mathcal{S}$. Compare this picture with the ones in the second row, where we fix two parameters at the correct values, but vary the third one. We set from left to right $X^s = X + \varepsilon^2 20\lambda_c$, $\ell^s = \ell/2.5$ and $\alpha^s = 2.5\alpha$. We observe that as we increase X the dispersion function is shifted to the right. We also observe that the variation in the parameters ℓ and α introduce a change in the form of the dispersion function. It is obvious, that the range X affects more the dispersion function than the other two parameters ℓ and α.

Remark 2 *It was shown in [10] that the range estimation methodology is not sensitive to the model that we use for the correlation function. In particular, for a medium with a Gaussian correlation function an exponential model was used instead and this did not affect the range estimation results. It affects however the estimation of the model parameters which may not be close to their true values when the wrong model for the correlation function is used.*

We illustrate next with numerical simulations that range estimation is robust in the incoherent zone, close to the equipartition distance and beyond this.

5.1.1 Range estimation results

We present here range estimation results, for the simulation setup described in section 4, for the two sources case and the variable sound speed profile. The bandwidth is $B = 62.5$Hz and $\Omega_d = 14.8$Hz.

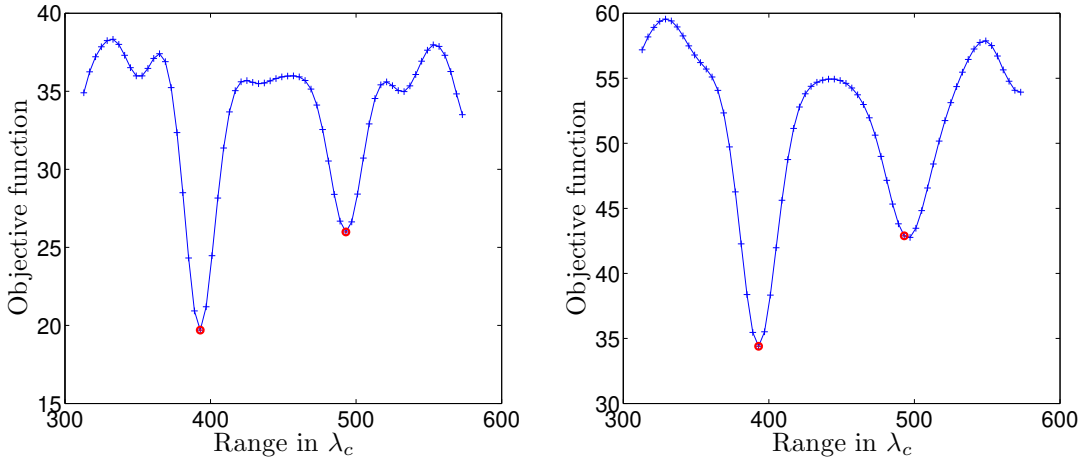

Figure 6: First pass of range estimation with $f_0 = 500$Hz, $\varepsilon = 2\%$ (left) and $f_0 = 887$Hz, $\varepsilon = 3\%$ (right). Data for two sources and the variable sound speed profile. The correct value of the sources' range is indicated with a red circle.

In Figure 6 we plot $\mathbb{O}_{\mathcal{D}}(X^s, \ell^s, \alpha^s)$ for the estimated values of $\ell^s = \ell^{\text{est}}$ and $\alpha^s = \alpha^{\text{est}}$ at $f_0 = 500$Hz with $\varepsilon = 2\%$ (close to the equipartition distance defined in Eq. (25), see also Figure 12-left) and $f_0 = 887$Hz with $\varepsilon = 3\%$ (beyond the equipartition distance, see Figure 12-right), over a range interval that contains both sources. The first pass is done by using a large range interval $[\chi_1, \chi_2] = [315, 575]\lambda_c\varepsilon^2$ with a step of $4\lambda_c\varepsilon^2$. The correct value of the sources' range is indicated with a red circle. In Figure 6 we show results for one realization of the random medium, however, similar results have been obtained for other realizations. The two minima we observe, indicate that we have two sources. We can locally compute $\mathbb{O}_{\mathcal{D}}(X^s, \ell^s, \alpha^s)$ around each source to determine their location more accurately. This is done by restricting the integral in Eq.(10) in range $(\varepsilon^{-2}\chi)$ at $\pm 30\lambda_c$ around each source with a step of λ_c.

In Figure 7 we show cross-sections of $\mathbb{O}_{\mathcal{D}}(X^s, \ell^s, \alpha^s)$ over these shorter range intervals that contain each source, separately. The correct values of (X, ℓ, α) are indicated with a red circle. In each plot we fix two parameters at the estimated values and display the variation in the third parameter. We show results for $f_0 = 500$Hz with $\varepsilon = 2\%$, and $f_0 = 887$Hz with $\varepsilon = 3\%$, for the data with the two sources and the variable sound speed profile. We observe that the range estimation is extremely robust even for the highest frequency in our bandwidth. The results are stable, that means that the estimated quantities do not fluctuate, when we change the realization of the random medium as illustrated by

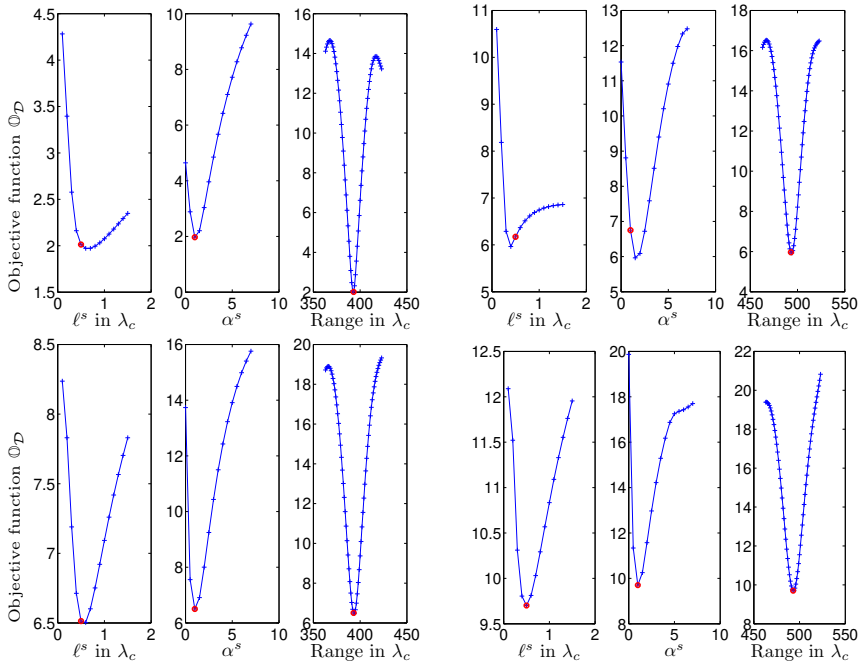

Figure 7: Cross-sections of the objective function $\mathbb{O}_{\mathcal{D}}$. First row: $f_0 = 500$Hz, $\varepsilon = 2\%$. Second row: $f_0 = 887$Hz, $\varepsilon = 3\%$. Data for two sources and the variable sound speed profile. Left: $\vec{x}_1^{\star}$. Right: $\vec{x}_2^{\star}$. The correct values of (X, ℓ, α) are indicated with a red circle.

the results in Figure 8(a) where we plot the estimated results for the source at $\vec{x}_1^{\star}$ for three realizations of the random medium. The results are similar for the source located at $\vec{x}_2^{\star}$.

Our results illustrate that we have a convex functional and therefore the minimization process is easy. In general, our objective functional has a clear minimum close to the correct values of the unknown parameters. The value of ℓ^{est} and α^{est} can be slightly off but this does not significantly affect the range estimation. Here we assumed a Gaussian model for the correlation function (see Eq.(5)) of the medium and searched for ℓ and α. As mentioned in Remark 2 the range estimation is not sensitive to the value of these parameters and can be successfully recovered even when the wrong model for the correlation function of the medium is used [3, 10].

To further illustrate the robustness of the range estimation we show in Figure 8(b) the results for the source at $\vec{x}_1^{\star}$, obtained for a vertical array with only 2 receivers located in the middle of the waveguide, at $9.8050\lambda_c$ and $10.1950\lambda_c$.

We observe that for the source at $\vec{x}_1^{\star}$ the range estimation continues to be accurate, although the parameters of the correlation function are slightly off. For the source at $\vec{x}_2^{\star}$ the range estimation has a 15% error and the correlation function parameters become ambiguous, so we do not show them here. If we decrease however f_0 to 400Hz, we recover the range for the source at $\vec{x}_2^{\star}$. Remember that for $\varepsilon = 3\%$ with $f_0 = 887$Hz, $\varepsilon^2 \mathcal{L}_{equip} \sim 200\lambda_c$ and with $f_0 = 400$Hz, $\varepsilon^2 \mathcal{L}_{equip} \sim 300\lambda_c$. The source at $\vec{x}_2^{\star}$ is $493\lambda_c$ far from the array, that is with $f_0 = 887$Hz we are already more than two times beyond the equipartition distance $\mathcal{L}_{equip}$ defined in Eq. (25) (see Figure 12-right).

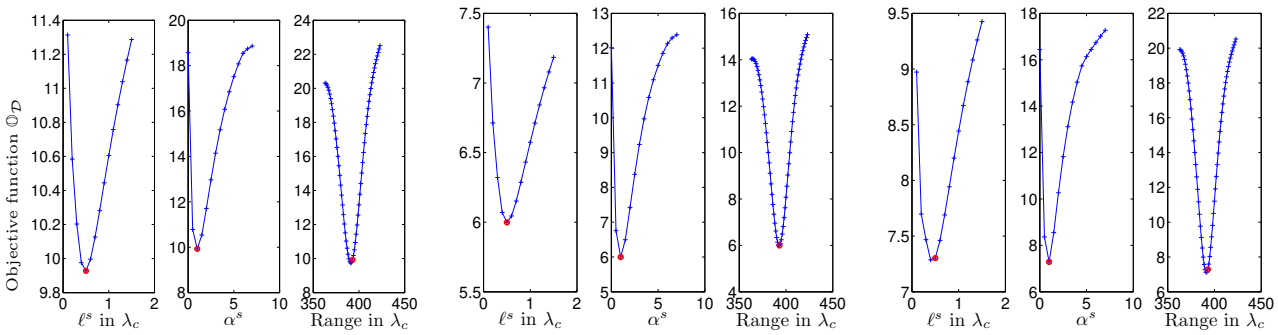

(a) Full array aperture results.

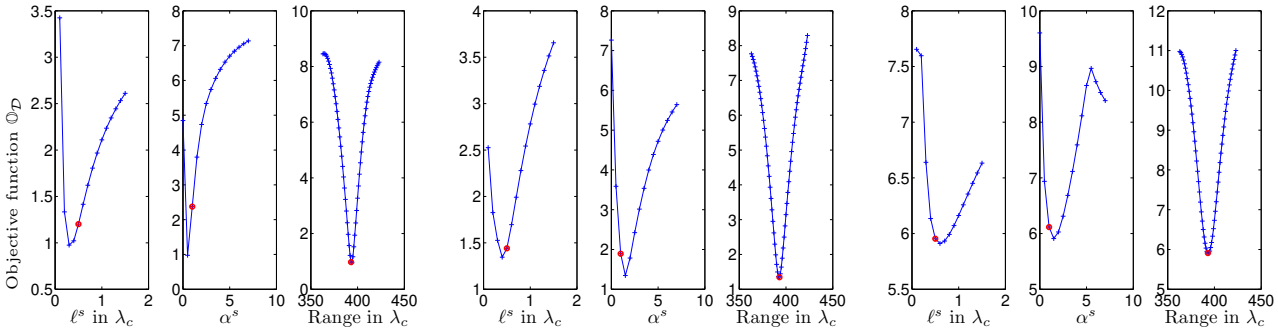

(b) Results obtained using only 2 receivers located at $9.8050\lambda_c$ and $10.1950\lambda_c$.

Figure 8: Cross-sections of the objective function $\mathbb{O}_{\mathcal{D}}$ for $\vec{x}_1^{\star}$ for three realizations of the random medium fluctuations. Data for two sources and the variable sound speed profile for $f_0 = 887$Hz and $\varepsilon = 3\%$. The correct values of (X, ℓ, α) are indicated with a red circle.

5.2 Depth estimation methodology

The depth estimation is more delicate than range estimation. We suppose that we have previously obtained an accurate estimate of the range X with the method described in Section 5.1.

First, we note that the Fourier coefficients of the depth profile $\widehat{\xi}_j$ do not depend on χ. This is because we assumed a source density of separable form. Moreover, we expect

$$\mathcal{D}_j^{obs}(\chi) \approx \mathcal{D}_j^{mod}(\chi; X^{\rm est}, \ell^{\rm est}, \alpha^{\rm est}) \tag{11}$$

due to the fact that $\mathcal{D}_j^{obs}(\chi)$ is close to its statistical mean by self-averaging. This is due to integration over frequencies and rapid statistical decorrelation over frequencies [11]. By integrating in range both parts of Eq.(11) and using Eq.(8) and Eq.(21), we get

$$\int_{\chi_1}^{\chi_2} d\chi \mathcal{D}_j^{obs}(\chi) := \mathcal{X}_j^{obs} \approx C \sum_{q,l=1}^{N} \frac{|\widehat{\xi}_l|^2}{\beta_l \beta_q} Q_{jq}^2 [e^{\Gamma X^{\rm est}}]_{jl}, \tag{12}$$

for $j = 1, \ldots N$. The constant C in Eq.(12) depends mainly on the pulse and the integration intervals used to define $\mathcal{D}_j(\chi)$ in Eq.(7). However, we do not need to know the value of C for the depth estimation since as we will see below we normalize by the average with respect to the modes in the objective function Eq.(16). The range interval over which we integrate the data in Eq.(12) is centered at the estimated range $X^{\rm est}$ and its width should be several wavelengths ($> 50\lambda_c$).

Using now the eigenvalue decomposition of Γ, we can write the following expression for the matrix exponential in Eq.(12)

$$e^{\Gamma X^{\text{est}}} = \sum_{j=1}^{N} e^{-|\Lambda_j| X^{\text{est}}} \mathbf{u}_j \mathbf{u}_j^T,$$

with Λ_j being the eigenvalues (energy conservation implies that $\Lambda_j \leq 0$) and $\mathbf{u}_j$ the eigenvectors of the matrix Γ.

We are interested in ranges beyond the equipartition distance, $X > \mathcal{L}_{equip} = 1/|\Lambda_2|$, and in this case we have

$$[e^{\Gamma X}]_{jl} = \sum_{r=1}^{N} e^{-|\Lambda_r| X} u_{jr} u_{lr} \approx \frac{1}{N},$$

where u_{jr} is the j-th component of the eigenvector $\mathbf{u}_r$. Thus, we can write Eq.(12) in the following form

$$\mathcal{X}^{obs} \approx \theta \, \mathbb{Q} \begin{pmatrix} 1/\beta_1 \\ \vdots \\ 1/\beta_N \end{pmatrix}, \qquad \theta = \frac{1}{N} \sum_{j=1}^{N} \frac{|\widehat{\xi}_j|^2}{\beta_j}, \tag{13}$$

where $\mathbb{Q}$ is the matrix with entries Q_{jl}^2 and Q_{jl} has been defined in Eq.(9). Remark that the matrix Q is the identity when the array spans the whole depth of the waveguide, due to the orthogonality of the modes. We observe that it is impossible to recover $|\widehat{\xi}_j|^2$ from Eqs.(13). Nevertheless, we can extract the weighted average θ from our processed data $\mathcal{X}^{obs}$ and write Eqs.(13) as

$$\theta \approx \frac{1}{N} (\beta_1, \ldots, \beta_N) \, \mathbb{Q}^{-1} \mathcal{X}^{obs}, \qquad \frac{|\widehat{\xi}_1|^2}{\beta_1} + \ldots + \frac{|\widehat{\xi}_N|^2}{\beta_N} = N\theta. \tag{14}$$

Considering now M different sub-bands with central circular frequencies ω_j, number of propagating modes $N_j := N(\omega_j)$ and $j = 1, \ldots, M$, we can obtain from Eqs.(14) the following system

$$\begin{bmatrix} 1/\beta_1(\omega_1) & \cdots & 1/\beta_{N_j}(\omega_j) & 0 & \cdots & 0 \\ \vdots & \ddots & & & & \\ 1/\beta_1(\omega_M) & \cdots & & & & 1/\beta_{N_M}(\omega_M) \end{bmatrix} \begin{pmatrix} |\widehat{\xi}_1|^2 \\ \vdots \\ |\widehat{\xi}_{N_M}|^2 \end{pmatrix} \approx \begin{pmatrix} N_1\theta_1 \\ \vdots \\ N_M\theta_M \end{pmatrix}. \tag{15}$$

This is an underdetermined system, since it has more unknowns than equations, $N_M > M$. Note that as we add sub-bands, we increase the number of equations and therefore we can hope for an improvement in our estimate of the unknowns.

Remark 3 *For a constant sound speed profile the eigenfunctions ϕ_j, $j = 1, \ldots, N$ do not depend on the frequency and therefore $\hat{\xi}_j$, $j = 1, \ldots, N$ as defined in Eq.(6) do not depend on ω_0. Consequently, the unknowns $|\hat{\xi}_j|^2$, $j = 1, \ldots, N_l$ are the same for all sub-bands corresponding to different central frequencies ω_l, $l = 1, \ldots, M$ and it is the higher frequency that determines the length of the unknown which is N_M. On the other hand the β_j's depend on frequency. Eq.(15) takes advantage of this remark. Since the unknowns $|\hat{\xi}_j|^2$, $j = 1, \ldots, N_M$ are the same for all frequency bands, we obtain a system with N_M unknowns and M equations. This approach will work only for constant or slowly varying ϕ_j over the bandwidth so that the assumption that the unknowns $|\hat{\xi}_j|^2$ are the same for all frequency bands holds.*

Assuming now that the depth profile of the source $\xi(z)$ is the indicator function of the interval $1_{[z^\star-\sigma/2,z^\star+\sigma/2]}$, we introduce the following model for its Fourier coefficients

$$\widehat{\xi}_j^{mod}(z^s,\sigma^s)=\frac{1}{\sigma^s}\int_{z^s-\sigma^s/2}^{z^s+\sigma^s/2}dz\phi_j(\omega_0,z).$$

We can recover $z^\star$ and σ by minimizing the following objective function, $\mathbb{O}_\xi(z^s,\sigma^s)$, which measures the misfit between the estimated $|\widehat{\xi}_j|^2$ and the model $|\widehat{\xi}_j^{mod}|^2$ values of the Fourier coefficients, divided by their average value over j to remove the unknown multiplicative constant C appearing in Eq.(12):

$$\mathbb{O}_\xi(z^s,\sigma^s)=\left\{\sum_{j=1}^{N}\left[\frac{|\widehat{\xi}_j^{mod}(z^s,\sigma^s)|^2}{\left\langle|\widehat{\xi}^{mod}(z^s,\sigma^s)|^2\right\rangle}-\frac{|\widehat{\xi}_j|^2}{\left\langle|\widehat{\xi}|^2\right\rangle}\right]^2\right\}^{1/2}. \tag{16}$$

In Eq.(16) we have used $\langle\cdot\rangle$ to denote the average of the numerators with respect to j,

$$\begin{aligned}\langle|\widehat{\xi}^{mod}(z^s,\sigma^s)|^2\rangle &= \frac{1}{N}\sum_{j=1}^{N}|\widehat{\xi}_j^{mod}(z^s,\sigma^s)|^2\\ \langle|\widehat{\xi}|^2\rangle &= \frac{1}{N}\sum_{j=1}^{N}|\widehat{\xi}_j|^2.\end{aligned}$$

When σ is very small we can write approximately

$$\widehat{\xi}_j^{mod}(z^s)\approx\phi_j(\omega_0,z^s)$$

and Eq.(16) takes the following form

$$\mathbb{O}_\xi(z^s)=\left\{\sum_{j=1}^{N}\left[\frac{|\phi_j(\omega_0,z^s)|^2}{\langle|\phi(\omega_0,z^s)|^2\rangle}-\frac{|\widehat{\xi}_j|^2}{\langle|\widehat{\xi}|^2\rangle}\right]^2\right\}^{1/2}, \tag{17}$$

so that we have only one parameter to estimate, the depth of the source z^s.

In the case of multiple sub-bands the objective function in Eq.(17) becomes

$$\mathbb{O}_\xi^M(z^s)=\left\{\sum_{j=1}^{N_M}\left[\frac{|\phi_j(\omega_M,z^s)|^2}{\langle|\phi(\omega_M,z^s)|^2\rangle}-\frac{|\widehat{\xi}_j|^2}{\langle|\widehat{\xi}|^2\rangle}\right]^2\right\}^{1/2}, \tag{18}$$

where we use $\langle\cdot\rangle$ as before to denote the average values of the numerators with respect to j. Note that for the multiple sub-bands we recover one vector of $|\hat{\xi}_j|^2$, $j=1,\ldots,N_M$ corresponding to the band with the higher central frequency ω_M and assuming that the ϕ_j are frequency independent the functional that we are using compares the recovered $|\hat{\xi}_j|^2$ with the corresponding ϕ_j in this band (M). We will examine next, how this estimation performs in our numerical simulation setup.

5.2.1 Depth estimation results

We consider here the method with the multiple sub-bands described above, for the depth estimation. More precisely, we estimate the Fourier coefficients of the depth profile by solving the ill-posed system of Eq.(15) via a least squares method using the MATLAB function Isqnonneg. Using the estimated

$|\widehat{\xi}_j|^2$ in Eq.(18) we obtain an estimate for the depth location of the source. The range interval over which we integrate the data in Eq.(12) to obtain $\mathcal{X}_j^{obs}$ is $[\chi_1, \chi_2] = [X^{\text{est}} - 30\lambda_c\varepsilon^2, X^{\text{est}} + 30\lambda_c\varepsilon^2]$. In each sub-band, the bandwidth is $B = 62.5$Hz and $\Omega_d = 14.8$Hz. In all plots of Figures 9 and 10 we indicate the correct values of the source locations with a vertical, red, dashed line.

First we show in Figure 9 results for one source located at $\vec{x}_2^{\star} = (5\lambda_c, 493\lambda_c)$, with $\varepsilon = 2\%$ and a constant sound speed profile. On the top row, the left plot corresponds to using one sub-band and as we can see the result is quite bad. However by increasing the number of sub-bands used, the objective function becomes less ambiguous and very good results are obtained for six or seven sub-bands (center and right plots on the second row of Figure 9). The two minima of the objective function $\mathbb{O}_{\xi}^{M}(z^s)$ on the bottom right plot of Figure 9 correspond to the source's depth at $5\lambda_c$ and its mirror location with respect to the center of the waveguide. Note that we cannot uniquely recover the source location since from Eq.(15) we recover $|\xi_j|$ and not ξ_j.

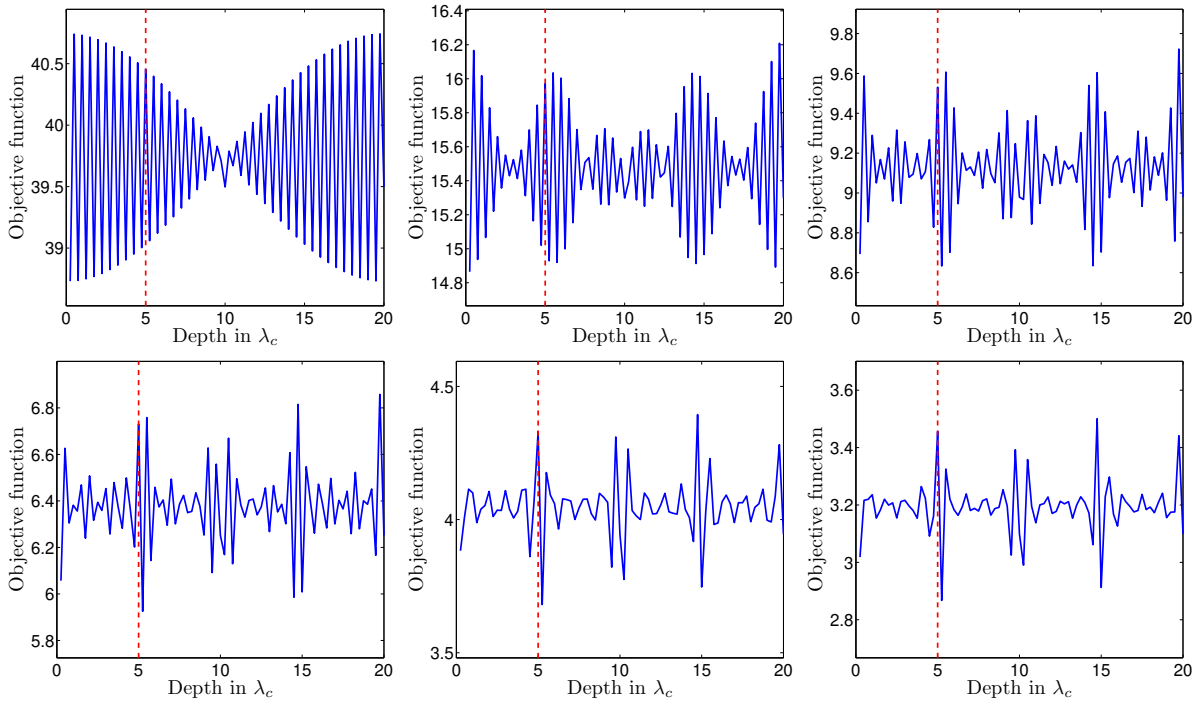

Figure 9: The objective function $\mathbb{O}_{\xi}^{M}(z^s)$, with $f_{j+1} = f_j + 50$Hz, for $j = 1, \ldots, M-1$. First row: $f_1 = 500$Hz, $M = 1$ (left), $M = 2$ (middle), $M = 3$ (right). Second row: $M = 4$, $f_1 = 500$Hz (left), $M = 6$, $f_1 = 500$Hz (middle), $M = 7$, $f_1 = 450$Hz (right). Data for one source at $\vec{x}_2^{\star}$, with $\varepsilon = 2\%$ and a constant sound speed profile. The correct values of the source locations are indicated with a vertical, red, dashed line.

In Figure 10(a), we show the results for the data with the two sources and $\varepsilon = 3\%$ for the case of a constant sound speed profile. The results with $\varepsilon = 2\%$ are similar, so we do not show them here. We observe that the method finds the location of the sources up to the symmetric ghost that we obtain similarly to the one source case. For the partial array aperture case the inversion of the matrix $\mathbb{Q}$ needed in Eq.(14) is performed using the regularized pseudoinverse.

Finally, in Figure 10(b), we show the results for the data with the two sources and $\varepsilon = 3\%$ for the case of the variable sound speed profile. We observe that now the method correctly locates the source at $\vec{x}_2^{\star}$ but not the one at $\vec{x}_1^{\star}$, even though this is the one closer to the array. This may be due to the sound

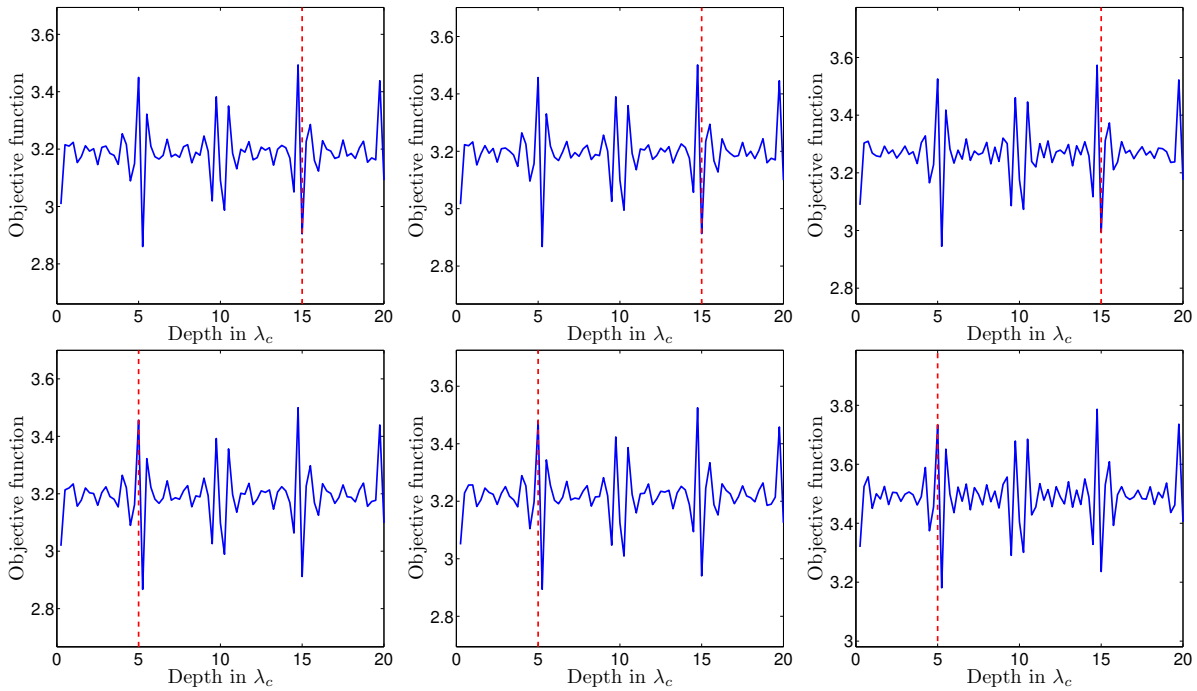

(a) Results for the constant sound speed profile and 3% fluctuations.

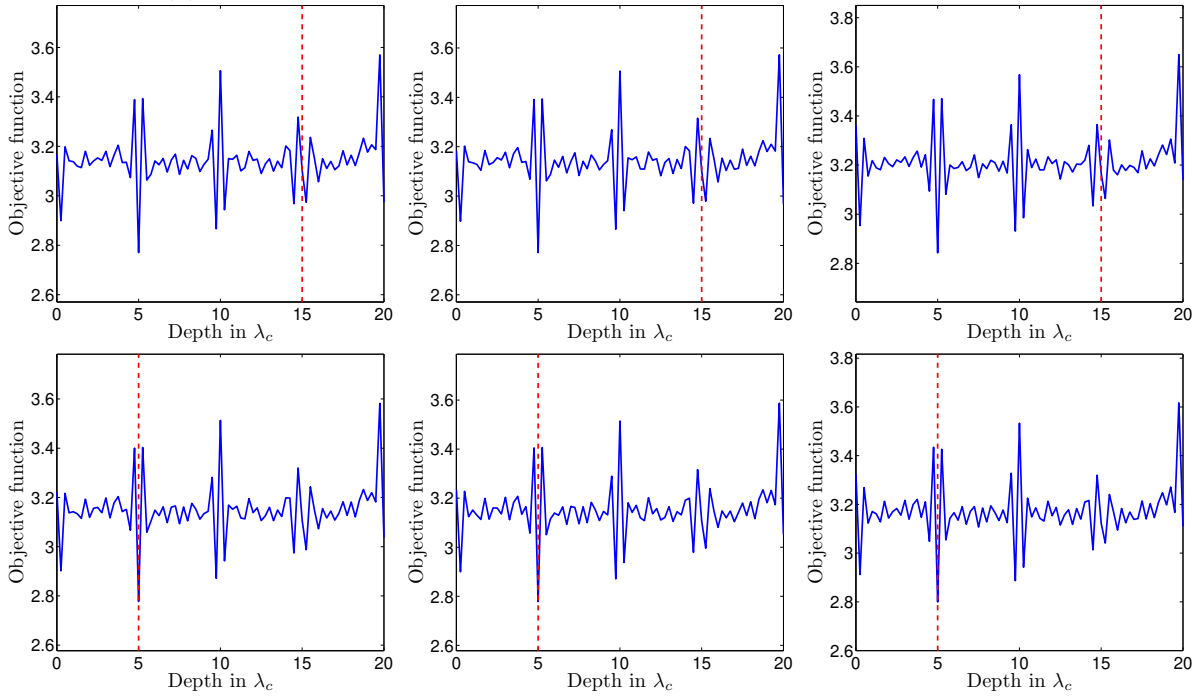

(b) Results for the varriable sound speed profile and 3% fluctuations.

Figure 10: The objective function $\mathbb{O}_{\xi}^{M}(z^s)$, with $f_{j+1} = f_j + 50\text{Hz}$, for $j = 1, \ldots, M-1$ with $M = 7$ and $f_1 = 450\text{Hz}$. From left to right: results obtained with full array aperture, half array aperture and using an array with 11 receivers located at the center of the waveguide. In each sub-figure the first row is for $\vec{x}_1^{\star}$ and the second row for $\vec{x}_2^{\star}$. The correct values of the source locations are indicated with a vertical, red, dashed line.

speed profile we have used which destroys the symmetry and guides the energy towards the bottom of the waveguide [17]. Note also that in this case the eigenfunctions ϕ_j depend on the frequency and therefore Eq.(15) holds only approximately (see also Remark 3). It is remarkable that we obtain very good results using only partial array aperture as shown in the results of Figure 10, where we decrease the number of receivers successively from 201 to 101 and 11 by removing array elements symmetrically from the top and the bottom.

To resume, this multiple band approach which requires a large bandwidth seems to be quite robust and gives a good estimation for the depth of point-like sources, close to and beyond the equipartition distance.

6 Discussion

In this work we consider a water column with small inhomogeneities in the index of refraction which can be due to internal waves. For convenience, we use a simple model of random ocean with flat and horizontal boundaries, depth/range isotropy and no attenuation. We want to focus on the saturated regime where acoustic waves have lost their initial state because of strong scattering. We chose the correlation length to be of the order of the wavelength so that we can reach the saturation regime at a relative short propagation distance of the order of hundreds of wavelengths.

To make this more precise we show in Figure 11 how the correlation length of the fluctuations affects the scattering mean path and the equipartition distance (see also Figure 12 in Appendix A). For a correlation length of the order of ten wavelengths, as is the case in the ocean, we will have to consider the array at very large distance from the sources in order to investigate the performance of the incoherent method in the equipartition regime (see the right plot in Figure 11). This would be extremely expensive in terms of computational time and memory requirements. Considering correlation lengths of the order of the wavelength, we reach the saturated regime at smaller propagation distances.

Both range and depth estimations have been tested extensively for different realizations of the random medium fluctuations. The accuracy of the estimation is of the order λ_c for the range and $\lambda_c/4$ for the depth. Range estimation uses one frequency band (sub-band) with small bandwidth $B = 62.5$Hz. Depth estimation requires multiple sub-bands which corresponds to effectively using a larger bandwidth ($B = 187.5$Hz and $B = 212.5$Hz for $M = 6$ and $M = 7$ bands, respectively). The results obtained by the incoherent methodology are robust and reliable. There is a significant improvement compared to the coherent imaging results shown in Section 4. To make our model more realistic we should consider in the future depth/range anisotropy and attenuation.

7 Conclusion

In this work we exhibited the performance of the incoherent methodology proposed and analyzed in [3, 11], for multiple source localization in a two dimensional acoustic waveguide with random inhomogeneities in the bulk medium.

We have seen that the incoherent approach for the range estimation of the source is very robust and gives accurate and reliable results even in the case where the distance between the source and the array is beyond equipartition, that is the distance at which energy is uniformly distributed between the modes, independently of the initial state. The estimation of the source's depth is more delicate. It requires knowledge of the source's range which has to be estimated first and a larger bandwidth compared to the range estimation.

Both range and depth estimations results are reliable and statistically stable, that means that they are independent of the realization of the random medium considered. Our numerical simulations

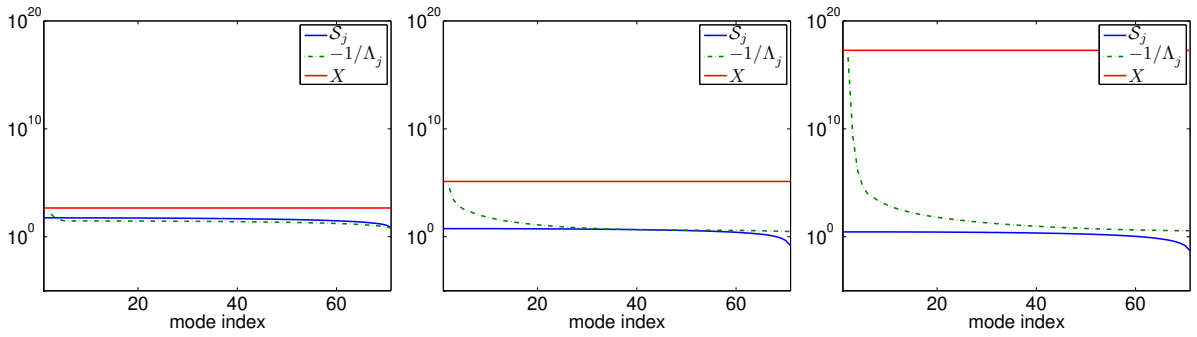

Figure 11: The scales $-1/\Lambda_j(\omega_0)$, for $j = 2, \ldots, N(\omega_0)$, the scattering mean free paths $\mathcal{S}_j(\omega_0)$, for $j = 1, \ldots, N(\omega_0)$ and the scaled range of an hypothetical source at $X = 2\mathcal{L}_{equip}(\omega_0)$, with $f_0 = 887$Hz and $\varepsilon = 3\%$. Left: $\ell = 0.5\lambda_c$, $X = 466.4\lambda_c\varepsilon^{-2}$. Middle: $\ell = 5\lambda_c$, $X = 1.331 \cdot 10^5\lambda_c\varepsilon^{-2}$. Right: $\ell = 10\lambda_c$, $X = 1.897 \cdot 10^{17}\lambda_c\varepsilon^{-2}$. Constant sound speed profile. The ordinate is in $\lambda_c\varepsilon^{-2}$.

illustrate the potential of the approach for underwater acoustic applications.

Acknowledgements

The work of C. Tsogka was partially supported by the European Research Council Starting Grant Project ADAPTIVES-239959 and the AFOSR grant FA9550-17-1-0238. This work was partially carried out while C. Tsogka was visiting the Mathematics Department at Stanford University and was supported by the AFOSR grant FA9550-11-1-0266. E. Karasmani worked as a PhD student for the project ADAPTIVES at IACM in FORTH. The work of L. Borcea was partially supported by NSF DMS-1510429.

References

[1] Flatté S, Tappert F. Calculation of the effect of internal waves on oceanic sound transmission. J Acoust Soc Am. 1975;58(6):1151–1159.

[2] Flatté S, Dashen R, Munk W, Watson K, Zachariassen F. Sound transmission through a fluctuating ocean. Cambridge, UK: Cambridge Univ.; 1979.

[3] Borcea L, Issa L, Tsogka C. Source localization in random acoustic waveguides. SIAM Multiscale Modeling and Simulation. 2010;8(5):1981–2022.

[4] Dozier LB, Tappert F. Statistics of normal mode amplitudes in a random ocean. J Acoust Soc Am. 1978;63(2):353–365.

[5] Colosi J, the ATOC Group. A review of recent results on ocean acoustic wave propagation in random media: basin scales. IEEE J Ocean Eng. 1999;24(2):138–155.

[6] Creamer D. Scintillating shallow-water waveguides. J Acoust Soc Am. 1996;99(5):2825–2838.

[7] Colosi J. Statistics of normal mode amplitudes in an ocean with random sound-speed perturbations: Cross-mode coherence and mean intensity. J Acoust Soc Am. 2009;126(3):1026–1035.

[8] Colosi JA. Sound propagation through the stochastic ocean. Cambridge University Press; 2016.

[9] Borcea L, Garnier J, Tsogka C. A quantitative study of source imaging in random waveguides. Commun Math Sci. 2015;13(3):749–776.

[10] Issa L. Imaging in cluttered acoustic waveguides [dissertation]. Rice University; 2010.

[11] Acosta S, Alonso R, Borcea L. Source estimation with incoherent waves in random waveguides. Inverse Problems. 2015;31(3):p.035013.

[12] Kohler W, Papanicolaou G. Sound propagation in a randomly inhomogeneous ocean. In: Keller JB, Papadakis J, editors. Wave propagation in underwater acoustics; Lecture notes in Physics; Vol. 70. Berlin: Springer-Verlag; 1977. p. 153–223.

[13] Fouque JP, Garnier J, Papanicolaou G, Sølna K. Wave propagation and time reversal in randomly layered media. Springer; 2007.

[14] Garnier J, Papanicolaou G. Pulse propagation and time reversal in random waveguides. SIAM J Appl Math. 2007;67(6):1718–1739.

[15] Garnier J, lna KS. Effective transport equations and enhanced backscattering in random waveguides. SIAM J Appl Math. 2008;68(6):1474–1599.

[16] Borcea L, Garnier J. Paraxial coupling of propagating modes in three-dimensional waveguides with random boundaries. SIAM Multiscale Modeling and Simulation. 2014;12(2):832–878.

[17] Hermand JP, Gerstoft P. Inversion of broad-band multitone acoustic data from the yellow shark summer experiments. IEEE J Ocean Eng. 1996;21(4):324–346.

[18] Borcea L, Karasmani E, Tsogka C. Underwater source detection and localization with incoherent data. In: Papadakis J, Bjørnø L, editors. Proceedings of the 3rd Underwater Acoustic Conference and Exhibition, Platanias, Crete, Greece; 2015. p. 829–834.

[19] Hegewisch K, Tomsovic S. Constructing acoustic timefronts using random matrix theory. J Acoust Soc Am. 2013;134(4):3174–3184.

[20] Borcea L, Papanicolaou G, Tsogka C. Interferometric array imaging in clutter. Inverse Problems. 2005;21:1419–1460.

[21] Borcea L, Papanicolaou G, Tsogka C. Adaptive interferometric imaging in clutter and optimal illumination. Inverse Problems. 2006;22(4):1405–1436.

[22] Borcea L, Papanicolaou G, Tsogka C. Asymptotics for the space-time Wigner transform with applications to imaging. In: Baxendale PH, Lototsky SV, editors. Stochastic differential equations: Theory and applications. volume in honor of professor boris l. rozovskii. Vol. 2 of Interdisciplinary Mathematical Sciences; World Scientific; 2007. p. 91–112.

[23] Baggeroer AB, Kuperman WA, Mikhalevsky PN. An overview of matched field methods in ocean acoustics. IEEE J Ocean Eng. 1993;18:401–424.

[24] Lin YT, Newhall AE, Lynch JF. Low-frequency broadband sound source localization using an adaptive normal mode back-propagation approach in a shallow-water ocean. J Acoust Soc Am. 2016;131:1798–1813.

[25] Bécache E, Joly P, Tsogka C. An analysis of new mixed finite elements for the approximation of wave propagation problems. SIAM J Numer Anal. 2000;37(4):1053–1084.

[26] Bérenger J. A perfectly matched layer for the absorption of electromagnetic waves. Journal of Comp Physics. 1994;114:185–200.

[27] Devroye L. Non-uniform random variate generation. Springer; 1986.

[28] Ripley B. Spatial statistics. Wiley; 1981.

A The Asymptotic Model

We explain in this section our asymptotic model for describing the acoustic pressure field recorded on the array. We first review the case of the unperturbed waveguide with velocity $c_0(z)$ and then we consider the random waveguide case.

A.1 The case of the unperturbed waveguide

We know that for the unperturbed velocity profile $c_0(z)$, and for a point harmonic source, energy is transmitted by independent guided modes so that the following model can be obtained.

We introduce $\lambda_j(\omega)$ the eigenvalues and $\phi_j(\omega, z)$ the orthogonal eigenfunctions of the symmetric differential operator $\partial_z^2 + \omega^2/c_0^2(z)$ with a Dirichlet boundary condition at the top of the waveguide $z = 0$ and a Neumann boundary condition at the bottom $z = H$. The wavenumbers, $\beta_j(\omega)$, are given by

$$\beta_j(\omega) = \begin{cases} \sqrt{\lambda_j(\omega)}, & j = 1, 2, \dots N(\omega), \\ \sqrt{-\lambda_j(\omega)}, & j > N(\omega), \end{cases}$$

where $N(\omega)$ is the number of propagating modes at frequency ω. The modes indexed by $j > N(\omega)$ are evanescent. In this case the acoustic pressure field recorded on the array and due to a point source at (x', z') is

$$p_0(t, x_{\mathcal{A}}, z_r) \approx \int d\omega \frac{\widehat{f}(\omega)}{2\pi} \sum_{j=1}^{N(\omega)} \frac{a_{j,0}^+(\omega, z')}{\sqrt{\beta_j(\omega)}} \phi_j(\omega, z_r) e^{i\beta_j(\omega)(x_{\mathcal{A}} - x') - i\omega t},$$

which is a superposition of propagating modes obtained by neglecting the evanescent modes for $j > N(\omega)$ since the array is far from the source. The amplitude of the modes $a_{j,0}^+$ does not depend on the range and is given by

$$a_{j,0}^+(\omega, z') = \frac{1}{2i\sqrt{\beta_j(\omega)}} \phi_j(\omega, z'). \tag{19}$$

When the background speed c_0 is constant, the number of propagating modes is $N(\omega) = \left\lfloor \frac{\omega H}{c_0 \pi} + \frac{1}{2} \right\rfloor$ and we have, for $j = 1, 2, \dots N(\omega)$,

$$\lambda_j(\omega) = \left(\frac{\omega}{c_0}\right)^2 - \left(\frac{\pi(j - 1/2)}{H}\right)^2, \quad \phi_j(z) = \sqrt{\frac{2}{H}} \sin\left(\frac{\pi(j - 1/2)z}{H}\right).$$

For a depth dependent wave speed $c_0(z)$, we do not know in general the analytic expression for the eigenvalues $\lambda_j(\omega)$ and the eigenfunctions $\phi_j(\omega, z)$ but we can always compute them numerically.

A.2 The case of random waveguides

Assuming now one extended source and following [13] and [11] we can write the Fourier coefficients of the random pressure field at frequency ω, recorded at the receivers $(x_{\mathcal{A}}, z_r)$ as

$$\widehat{p}^{\varepsilon}(\omega, x_{\mathcal{A}}, z_r) \approx \int \int_{\Omega_\rho} dx' dz' \rho(x', z') \widehat{f}^{\varepsilon}(\omega) \sum_{j=1}^{N(\omega)} \frac{a_j^+(\omega, X/\varepsilon^2, x', z')}{\sqrt{\beta_j(\omega)}} \phi_j(\omega, z_r) e^{i\beta_j(\omega)(x' - X/\varepsilon^2)},$$

where we introduced the scaled range $X = \varepsilon^2 |x^\star - x_{\mathcal{A}}|$ and the forward random amplitudes a_j^+, for $j = 1, \dots N(\omega)$, given by

$$a_j^+(\omega, X/\varepsilon^2, x', z') = \sum_{l=1}^{N(\omega)} \frac{1}{2i\sqrt{\beta_l(\omega)}} \phi_l(\omega, z') T_{jl}^{\varepsilon}(\omega, X, x').$$

Note that we have also scaled the bandwidth B relative to ε at central frequency $\omega_0 = 2\pi f_0$ and define

$$\widehat{f}^{\varepsilon}(\omega) = \frac{1}{\varepsilon^{\mu}} \widehat{f}\left(\frac{\omega - \omega_0}{\varepsilon^{\mu}}\right),$$

for $1 < \mu \leq 2$. The scaling is performed with respect to the small parameter ε that controls the strength of the fluctuations of the random medium Eq.(2). The difference with respect to the unperturbed waveguide case is that the mode amplitudes $\mathbf{a}^{\varepsilon} = \left(a_1^+, \ldots a_{N(\omega)}^+\right)^T$ are random functions that depend also on the range (not only on frequency and z' as in Eq.(19)) and satisfy the following system of linear stochastic differential equations (see also [13, 3])

$$\begin{aligned} \frac{\partial}{\partial x}\mathbf{a}^{\varepsilon}(\omega, x) &= \left[\frac{1}{\varepsilon}\mathbb{P}^{(a,a)}\left(\omega, \frac{x}{\varepsilon^2}\right) + \mathbb{E}^{(a,a)}\left(\omega, \frac{x}{\varepsilon^2}\right)\right]\mathbf{a}^{\varepsilon}(\omega, x), \qquad x > 0, \\ \mathbf{a}^{\varepsilon}(\omega, 0) &= \mathbf{a}_0(\omega, z') = \left(a_{1,0}^+(\omega, z'), \ldots a_{N(\omega),0}^+(\omega, z')\right)^T. \end{aligned} \tag{20}$$

Since the stochastic differential equations (20) are linear, we can write

$$\mathbf{a}^{\varepsilon}(\omega, x) = \mathbf{T}^{\varepsilon}(\omega, x)\mathbf{a}_0(\omega, z'),$$

where $\mathbf{T}^{\varepsilon}$ is the transfer or propagator matrix and satisfies

$$\frac{\partial}{\partial x}\mathbf{T}^{\varepsilon}(\omega, x) = \left[\frac{1}{\varepsilon}\mathbb{P}^{(a,a)}\left(\omega, \frac{x}{\varepsilon^2}\right) + \mathbb{E}^{(a,a)}\left(\omega, \frac{x}{\varepsilon^2}\right)\right]\mathbf{T}^{\varepsilon}(\omega, x), \qquad x > 0,$$

with initial condition

$$\mathbf{T}^{\varepsilon}(\omega, 0) = I,$$

where I is the identity matrix.

The $N(\omega) \times N(\omega)$ matrices $\mathbb{P}^{(a,a)}$ and $\mathbb{E}^{(a,a)}$ are given by

$$\mathbb{P}_{jl}^{(a,a)}(\omega, x) = \frac{i\omega^2}{2\bar{c_0}^2} \frac{\nu_{jl}(x)}{\sqrt{\beta_j(\omega)\beta_l(\omega)}} e^{i[\beta_l(\omega) - \beta_j(\omega)]x},$$

and

$$\mathbb{E}_{jl}^{(a,a)}(\omega, x) = \frac{i\omega^4}{4\bar{c_0}^4} \sum_{l' > N(\omega)} \int_{-\infty}^{\infty} ds \frac{\nu_{jl'}(x)\nu_{ll'}(x+s)}{\beta_{l'}(\omega)\sqrt{\beta_j(\omega)\beta_l(\omega)}} e^{i\beta_l(\omega)(x+s) - i\beta_j(\omega)x - \beta_{l'}(\omega)|s|},$$

respectively, in terms of the random stationary processes

$$\nu_{jl}\left(\frac{x}{\ell}\right) = \int_0^H dz \, \frac{\bar{c_0}^2}{c_0^2(z)} \nu\left(\frac{x}{\ell}, \frac{z}{\ell}\right) \phi_j(\omega_0, z)\phi_l(\omega_0, z), \qquad j, l = 1, 2, \ldots \quad .$$

In the definition of ν_{jl}, $\bar{c_0}$ denotes a reference constant wave propagation speed, the same reference speed appears also in Eq.(22), while $c_0(z)$ is the depth dependent velocity profile. In the case of a constant sound speed profile in the water column, $c_0(z) \equiv \bar{c_0}$ and the ratio $\bar{c_0}^2/c_0^2(z)$ (index of refraction) is equal to 1.

In the asymptotic limit $\varepsilon \to 0$, the expectation of the transfer matrix is given by

$$\lim_{\varepsilon \to 0} \langle T_{jl}^{\varepsilon} \rangle = \delta_{jl} \, e^{-\frac{1}{\mathcal{S}_j(\omega)}X + i\frac{1}{\mathcal{L}_j(\omega)}X},$$

where δ_{jl} is the Kronecker delta symbol. The expectation of the mode amplitudes is

$$\lim_{\varepsilon\to 0}\langle a_j^+\rangle = \frac{1}{2i\sqrt{\beta_j(\omega)}}\,\phi_j(\omega,z')\,e^{-\frac{1}{\mathcal{S}_j(\omega)}X+i\frac{1}{\mathcal{L}_j(\omega)}X},$$

where we recover the mode amplitude in the unperturbed waveguide $a_{j,0}^+$ multiplied by a factor that exponentially decays in range at the scale of $\mathcal{S}_j(\omega)$ and with a phase shift that increases with range on the scale $\mathcal{L}_j(\omega)$. We give below the definition of $\mathcal{S}_j(\omega)$ and refer to [9] for the definition of $\mathcal{L}_j(\omega)$ which is not needed in our computations. We denote by $\mathcal{S}_1(\omega_0)$ the scattering mean free path for the first mode which is the largest of all $\mathcal{S}_j(\omega_0)$. We consider in this paper ω_0 for which the array is at distance $X \geq \mathcal{S}_1(\omega_0)$ from the source. In that case we are in an incoherent regime and the source location cannot be determined by any method that relies on the coherent part of the pressure field. To successfully determine the source location we rely on an incoherent methodology that describes how energy propagates in the random waveguide.

We refer below to the results needed for the source localization. These are the second moments of the transfer matrix $\mathbf{T}^\varepsilon(\omega,X)$ at nearby frequencies. At large distances ($X > S_1$) the only second moments that remain large are the mean energies of the modes.

To obtain the behavior for the second moments of the modes amplitudes we need to study the two-frequency asymptotics of the propagator matrix. Thus we define

$$U_{jl}^\varepsilon(\omega,h,x) = T_{jm}^\varepsilon(\omega,x)T_{ln}^{\varepsilon *}(\omega-\varepsilon^2 h,x)$$

and its Fourier transform

$$V_{jl}^\varepsilon(\omega,\tau,x) = \frac{1}{2\pi}\int dh U_{jl}^\varepsilon(\omega,h,x)e^{-ih(\tau-\beta_l'(\omega)x)}.$$

Applying the diffusion approximation theorem we can obtain the limiting equation for V_{jl}^ε as $\varepsilon\to 0$ which satisfies the following system of transport equations

$$\left[\frac{\partial}{\partial x}+\beta_j'(\omega)\frac{\partial}{\partial\tau}\right]\mathcal{W}_j^{(l)}(\omega,\tau,x) = \sum_{n\neq j}\Gamma_{jn}(\omega)\left[\mathcal{W}_n^{(l)}(\omega,\tau,x)-\mathcal{W}_j^{(l)}(\omega,\tau,x)\right],\quad x>0,$$

with initial condition

$$\mathcal{W}_j^{(l)}(\omega,\tau,0) = \delta(\tau)\delta_{jl},$$

and $\delta(\tau)$ being a Dirac delta distribution.

This system describes the expectation of the energy of the j-th mode when the initial excitation is on the l-th mode. Its solution in the Fourier domain is given by

$$\widehat{\mathcal{W}}_j^{(l)}(\omega,h,x) = \int d\tau \mathcal{W}_j^{(l)}(\omega,\tau,x)e^{ih\tau} = [e^{[\Gamma(\omega)+ih\mathcal{B}'(\omega)]x}]_{jl} \tag{21}$$

with $\mathcal{B}'(\omega) = diag(\beta_1'(\omega),\ldots,\beta_N'(\omega))$ a diagonal matrix and $\beta_j'(\omega)$ the derivative of $\beta_j(\omega)$ with respect to ω. The matrix $\Gamma(\omega)$ depends on the frequency and the correlation function of the random fluctuations and can be written in the following form,

$$\begin{aligned}
\Gamma_{jl}(\omega) &= \frac{\omega^4\ell}{4\bar{c_0}^4\beta_j(\omega)\beta_l(\omega)}\widehat{\mathcal{R}}_{\nu_{jl}}\left[(\beta_j(\omega)-\beta_l(\omega))\,\ell\right],\quad j\neq l,\\
\Gamma_{jj}(\omega) &= -\sum_{l'\neq j,l'=1}^{N(\omega)}\Gamma_{jl'}(\omega),
\end{aligned} \tag{22}$$

for $j, l = 1, \ldots, N(\omega)$ and with $\widehat{\mathcal{R}}_{\nu_{jl}}$ the power spectral density of ν_{jl}

We can also define the scales $\mathcal{S}_j^P(\omega)$

$$\mathcal{S}_j^P(\omega) = -\frac{2}{\Gamma_{jj}(\omega)}, \tag{23}$$

and write for the scattering mean free paths

$$\frac{1}{\mathcal{S}_j(\omega)} = \frac{\omega^4 \ell}{8\bar{c_0}^4 \beta_j(\omega)} \sum_{l=1}^{N(\omega)} \frac{1}{\beta_l(\omega)} \widehat{\mathcal{R}}_{\nu_{jl}} \left[(\beta_j(\omega) - \beta_l(\omega))\, \ell \right]. \tag{24}$$

Let $\Lambda_j(\omega)$ be the eigenvalues of the matrix $\Gamma(\omega)$, in descending order, and $\mathbf{u}_j(\omega)$ the corresponding eigenvectors. Conservation of energy implies that all the eigenvalues are less or equal to zero. In the long range limit the matrix exponential

$$\mathbf{E}(\omega, x) = e^{\Gamma(\omega)x} = \sum_{j=1}^{N(\omega)} e^{\Lambda_j(\omega)x} \mathbf{u}_j(\omega) \mathbf{u}_j^T(\omega)$$

is determined by the null space of $\Gamma(\omega)$. Under the assumption that the power spectral density does not vanish for any of the arguments in Eq.(22), then $\Gamma(\omega)$ is a Perron-Frobenius matrix with simplest largest eigenvalue $\Lambda_1(\omega) = 0$ and the leading eigenvector is

$$\mathbf{u}_1(\omega) = \frac{1}{\sqrt{N}}(1, 1, \ldots, 1)^T.$$

As the propagation distance grows we have

$$\sup_{j,l=1,\ldots,N} \left| E_{jl} - \frac{1}{N} \right| \leq O(e^{\Lambda_2 x}),$$

which implies that the energy is uniformly distributed over the modes for distances

$$x \geq \mathcal{L}_{equip}(\omega) := -1/\Lambda_2(\omega), \tag{25}$$

where we introduced the equipartition distance $\mathcal{L}_{equip}(\omega)$.

To illustrate in which regime our numerical simulations have been carried out in terms of these length scales, we plot in Figure 12 the eigenvalues $-1/\Lambda_j(\omega_0)$, for $j = 2, \ldots, N$, the scales $\mathcal{S}_j^P(\omega_0)$ defined in Eq.(23) and the scattering mean free paths $\mathcal{S}_j(\omega_0)$ (see Eq.(24)) for $j = 1, \ldots, N$. We also plot the scaled ranges $X_1 = \varepsilon^2 |x_1^\star - x_{\mathcal{A}}|$ and $X_2 = \varepsilon^2 |x_2^\star - x_{\mathcal{A}}|$ for the sources at $\vec{x}_1^\star$ and $\vec{x}_2^\star$, respectively. We use either $f_0 = 500$Hz with $\varepsilon = 2\%$ or $f_0 = 887$Hz with $\varepsilon = 3\%$. We observe that X_1 and X_2 are above the scattering mean free paths in both plots. This means that we expect our data to be incoherent for $f_0 \geq 500$Hz and $\varepsilon \geq 2\%$. As we increase the frequency and the strength of the fluctuations ε, we expect our data to become more and more incoherent, since the distance between X_1 or X_2 and $\mathcal{S}_j$ increases. We also observe that for $\varepsilon = 3\%$, X_1 and X_2 are beyond the equipartition distance $-1/\Lambda_2(\omega_0)$, whereas for $\varepsilon = 2\%$, X_2 is close to this limit.

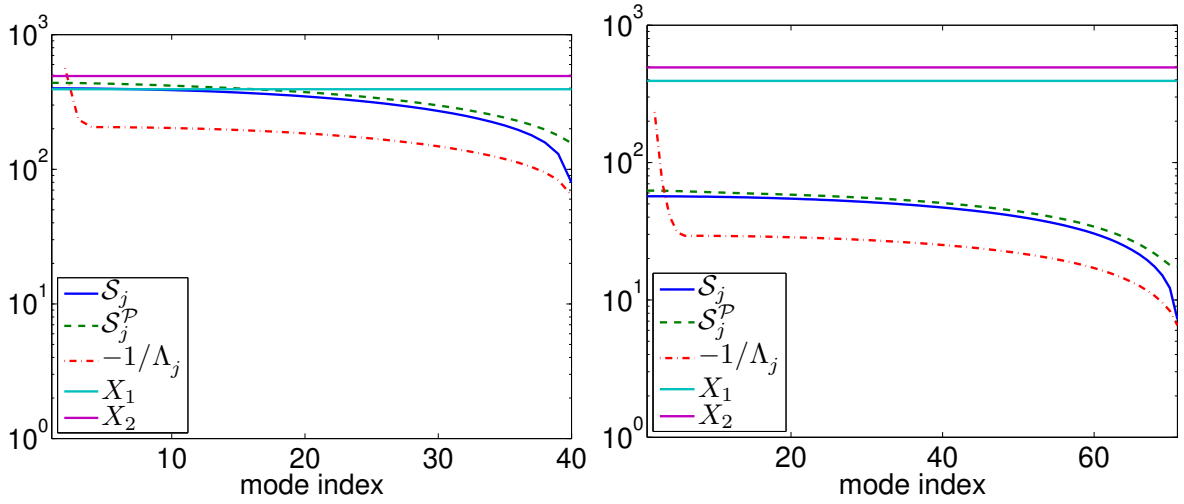

Figure 12: The scales $-1/\Lambda_j(\omega_0)$, for $j = 2, \ldots, N(\omega_0)$, $\mathcal{S}_j^P(\omega_0)$, the scattering mean free paths $\mathcal{S}_j(\omega_0)$, for $j = 1, \ldots, N(\omega_0)$ and the scaled ranges X_1 and X_2. Left: $f_0 = 500$Hz, $\varepsilon = 2\%$. Right: $f_0 = 887$Hz, $\varepsilon = 3\%$. Constant sound speed profile. The ordinate is in $\lambda_c \varepsilon^{-2}$.